34th Annual International Conference of the IEEE EMBS
San Diego, California USA, 28 August - 1 September, 2012

Positive contrast MRI of prostate brachytherapy seeds by susceptibility mapping

Ying Dong and Jim Ji

Department of Electrical and Computer Engineering, Texas A&M University

Abstract—**MRI can provide high-resolution images to assist physicians during intraoperative and post-operative phases of prostate brachytherapy. However, the brachytherapy seeds usually show as dark spots, i.e. negative contrast, on the MRI images. In this paper, we propose a new method to generate positive contrast seed images by mapping their susceptibility. The method is based on an improved kernel deconvolution algorithm using l_1 regularization. Simulation results show the positive contrast seeds can be identified and differentiated using the proposed method.**

I. Introduction

Prostate brachytherapy treats cancer by directly inserting radioactive material into the tissue to provide highly localized radiations to kill malignant cells [1-2]. Ultrasound imaging is typically used to provide a means to monitor and evaluate the intraoperative and post-operative phases of prostate brachytherapy. Recently, MRI has been explored as an alternative imaging modality that can provide physicians with high-resolution, more accurate information in such procedures.

In MRI, brachytherapy seeds normally show as dark spots due to the lack of hydrogen protons in the principally metallic seeds, which makes it difficult to differentiate the seeds from the cavities/voids in the tissue or susceptibility artifacts in the image, especially in low signal intensity areas. This hinders the seed detection and quantification of radiation doses. Our group has proposed to use off-resonance excitation to generate positive MRI of brachytherapy seeds[2]. However, spatial-spectrally selective off-resonance pulses are required to achieve the positive contrast.

In this paper, we propose an alternative method to the previous work in [2] for the positive contrast brachytherapy seed MRI. The method is based on susceptibility mapping, similar to the one used in quantitative susceptibility-weighted imaging (SWI) [3]. Specifically, an improved kernel deconvolution algorithm using l_1 regularization is developed to extract susceptibility map from a sequence of images acquired at different echo time. Computer simulations are used to test the proposed methods.

Ying Dong and Jim Ji are with the Department of Electrical and Computer Engineering, Texas A&M University, College Station, TX 77843-3128 USA (corresponding author: Jim Ji, phone: 979-458-1468; fax: 979-845-6259; e-mail: jimji@tamu.edu).

II. Theory and Method

In MRI, the local magnetic field can be approximated as the convolution of the susceptibility distribution with a kernel which is the response of a dipole [4].

$$\Delta B(r) = \frac{3\cos^2(\theta_r)-1}{4\pi r^3} \otimes \chi(r) \tag{1}$$

where $\Delta B(r)$ is the field inhomogeneity, $\chi(r)$ is the spatial susceptibility distribution, r is the distance between the observer and origin, and θ_r is the azimuthal angle [5].

Eq.(1) is a continuous-time relationship. However, only limited number of data is sampled in MRI. Therefore, a discretization is needed to calculate the field map.

$$\Delta \mathbf{B}(\mathbf{r}) = \frac{3\cos^2(\boldsymbol{\theta}_\mathbf{r})-1}{4\pi \mathbf{r}^3} \otimes \boldsymbol{\chi}(\mathbf{r}) \tag{2}$$

The Fourier transform of the dipole kernel is $(\frac{1}{3}-\frac{\mathbf{k}_z^2}{\mathbf{k}^2})$ [6], according to the convolution theorem, Eq.(2) can be transformed to

$$\mathcal{F}(\boldsymbol{\chi}(\mathbf{r}))\cdot(\frac{1}{3}-\frac{\mathbf{k}_z^2}{\mathbf{k}^2}) = \mathcal{F}(\Delta\mathbf{B}(\mathbf{r})) \tag{3}$$

where $\mathbf{k}^2 = \mathbf{k}_x^2 + \mathbf{k}_y^2 + \mathbf{k}_z^2$, $\mathbf{k}_* = \frac{2\pi}{FOV_*} * \mathbf{n}_*$, where FOV_* are the field of view in each direction, and $\mathbf{n}_*$ denotes the index of the pixel in each direction respect to the center of the sampling matrix. And $\cdot$ denotes the point-wise multiplication.

However, the Fourier transform of the kernel is 0 and irreversible when $\mathbf{k}^2 = 3\mathbf{k}_z^2$. To choose $\mathbf{k}_x$, $\mathbf{k}_y$ and $\mathbf{k}_z$ so as to avoid 0 when discretized can avoid the ill-poseness, but result in ill-condition [7-8]. To overcome this problem, regularizations are required.

1. L1 regularization

Rewrite Eq. (2) as

$$\boldsymbol{\psi} = \mathbf{C}\boldsymbol{\chi} \tag{4}$$

where $\boldsymbol{\chi}$ is the discretized susceptibility distribution, $\mathbf{C}$ is the operator denotes the convolution with the kernel, and $\boldsymbol{\psi}$ is the discretized field map. In practice, the field map can be

obtained from the phase information embedded in a sequence of T2-weighted images acquired at different echo time [8].

Since the number and size of the brachytherapy seeds are small, the brachytherapy seed MRI images can be considered sparse. Therefore, l_1 norm is appropriate for the regularization and the susceptibility mapping is achieved by

$$\min_{\chi} \|\mathbf{G}\chi\|_1 \quad \text{subject to } \|\mathbf{M}(\mathbf{C}\chi - \psi)\|_2 \le \varepsilon \tag{5}$$

where $\mathbf{G}$ denotes the first order gradient operator to enhance smoothness, $\mathbf{M}$ is the masking matrix which eliminates the background regions in the data, and ε is a small constant which is determined based on the noise level.

The masking matrix $\mathbf{M}$ is designed to utilize only the useful and reliable information around the seed. The seed itself is mask out because it has no spins and the magnitude is very low, therefore the phase information is not reliable. $\mathbf{M}$ can be calculated by setting a threshold to the local phase variance since the phase distribution in the background and seeds is much random than that of the tissue regions.

Rewrite Eq.(5) into Lagrangian form. Since we don't care about the exact value of the objective value, we put the Lagrangian multiplier λ in front of the constraint instead of the objective function, in according to many MRI related L1 minimization references [5, 8-9].

Within the mask region defined by $\mathbf{M}$, the signal is much stronger than the noise, therefore ε would be a very small number which is neglect for simplicity. After these steps, the problem in Eq.(5) can be reformulated as

$$\min_{\chi} \|\mathbf{M}(\mathbf{C}\chi - \psi)\|_2^2 + \lambda \|\mathbf{G}\chi\|_1 \tag{6}$$

where the first term controls the data consistency, and the second term promotes the sparsity. Problem (6) can be solved by setting the first order gradient respect to χ to 0.

$$\nabla f(\chi) = 2\mathbf{C}^H\mathbf{M}^H(\mathbf{M}(\mathbf{C}\chi - \psi)) + \lambda\nabla\|\mathbf{G}\chi\|_1 = 0 \tag{7}$$

where ^{H} is the Hermitian conjugate of the operator/matrix. $\|\mathbf{G}\chi\|_1$ is not differentiable at 0, so a small number is added to make it differentiable [9]. The approximation of (7) is,

$$\nabla f(\chi) \approx 2\mathbf{C}^H\mathbf{M}^H(\mathbf{M}(\mathbf{C}\chi - \psi)) + \lambda\mathbf{G}^H\mathbf{W}^{-1}\mathbf{G}\chi \tag{8}$$

where W is a diagonal matrix with the diagonal elements $\omega_k = \sqrt{(\mathbf{G}\chi)_k^*(\mathbf{G}\chi)_k + \mu}$ where μ is a very small number. In this paper, μ is set to 10^{-15}. Parameters λ affects the reconstruction results. It is tuned by iteratively narrowed down the range from 10^{-10} to 10^{10}. Visually comparison is used to determine the reconstruction quality.

Eq. (8) can be solved using a nonlinear conjugate gradient method [9]. The introduction of $\mathbf{W}$ makes the matrix to be positive definite, so that the conjugate gradient method converge within a finite number of iterations.

2. Data preparation

To test the proposed method, a set of susceptibility weighted images was simulated. The image resolution was set to 1 mm in all three dimensions. Eight slices of 128*128 images were simulated. The size of the STM 1251 seeds (4.55mm long * 0.81mm diameter [10]) was used to simulate the seeds in axial orientation, which occupy approximately 1 pixel in 5 slices (3^{rd} to 7^{th} slices). Three seeds were placed in the field of view (FOV). The magnitude of background tissue is set to be 0.1, the magnitude of the seed is set to be 0. The susceptibility of the background tissue is set to be 0, and the susceptibility of the seeds is set to be 0.7 ppm.

The field map is calculated using Eq. (2), and the phase is calculated using $\varphi = \gamma B_0 TE\Delta B$, where TE is set to be 1ms. Then Gaussian noise is added to the real and imaginary part of the images separately with an effective the peak SNR of 100 (i.e. 20dB).

An experimental dataset is acquired using Varian 33cm with two STM 1251 dummy seeds. Spin-echo sequence with shifted 180 degree RF pulse, also known as Dixon method, is applied. The matrix size is 128*128*7. The FOV is 80mm*80mm. The TE is 30ms. The 180 RF pulse is shifted by T_{shift} [0, 0.1, 0.2, 0.3, 0.4, 0.5]ms towards the acquisition window. The phantom is made of gelatin, doped with copper sulfate. Two STM 1251 dummy seeds are placed inside the phantom. The phase is calculated using $\Delta B = \dfrac{\Delta\varphi}{2\gamma B_0 T_{shift}}$.

This deconvolution reconstruction procedure was performed offline using MATLAB (Math Works, Natick, MA). The nonlinear conjugate gradient method is developed in house based on SparseMRI [9]. The processor of the computer is Intel® Core™ 2 Duo CPU T8300 @2.40GHz, the RAM is 2GB, and the system is Windows 7 Ultimate. Multiple regularization parameters were tested and the best results are selected by visual comparison.

III. RESULTS

Fig. 1 shows the field map in the simulated image. The region around the seeds clearly shows the field inhomogeneity due to the susceptibility. Fig. 2 shows the phase map of the simulated susceptibility weighted image. The scale of the image is adjusted so that the ringing artifact can be visualized clearly. Due to the noise, the phase of the three seeds and their surroundings is not exactly the same.

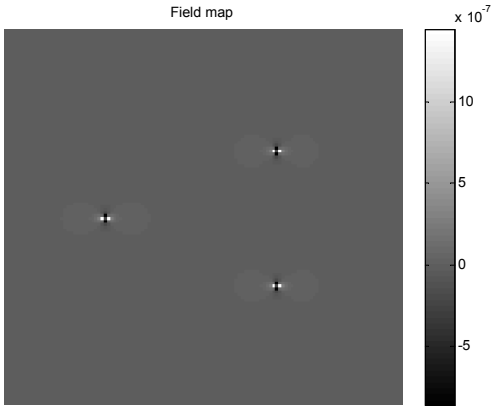

Fig.1 The field map of the simulated data set.

Fig. 3 shows the obtain susceptibility map from the noisy MRI images using the proposed method. Clearly, the seeds

show as positive contrast spots, reflecting a rather accurate susceptibility mapping.

Fig. 4 shows the coronal view of the phase image and the susceptibility map of one representative seed. The field inhomogeneity around the seed in the upper image is removed and the shape of the seed is clearly shown in the susceptibility map.

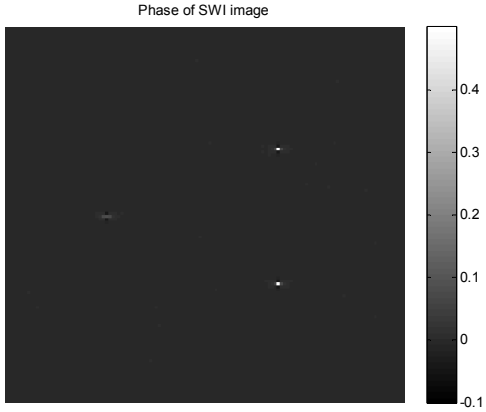

Fig.2 The phase of the simulated data set.

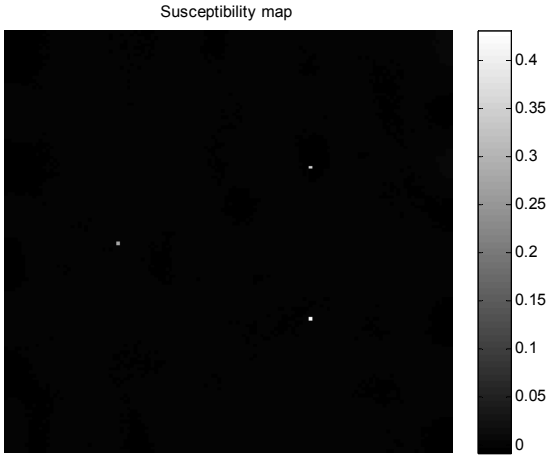

Fig.3 The susceptibility map obtained using the proposed method (axial view).

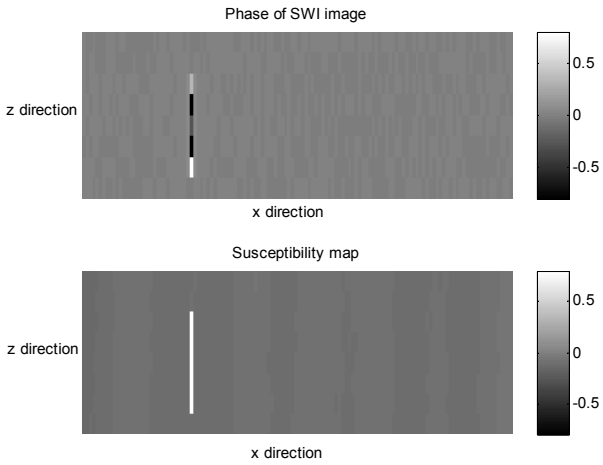

Fig.4 The phase image (up) and its susceptibility map (down) of a seed using the proposed method (coronal view)

Fig. 5 shows the magnitude and the phase image of the experimental data in the center slice with different Tshift. With Tshift = 0ms, there is no obvious difference between the seeds and the gelatin in the phase image. This is because the spin echo sequence can avoid the phase caused by field inhomogeneity. But when the 180 degree RF pulse is shifted, the spins cannot be refocused and the phase due to field inhomogeneity is shown in the phase, without affecting the magnitude image much.

Fig. 6 shows the field map of the experimental data in the center slice. A mask is applied to avoid the background noise. An increase in field strength in the seeds and a decrease around the seed is clear seen in the field map.

Fig. 7 shows the susceptibility calculated using the proposed method. Compared with the field map, the susceptibility shows better localization and good contrast in the gelatin.

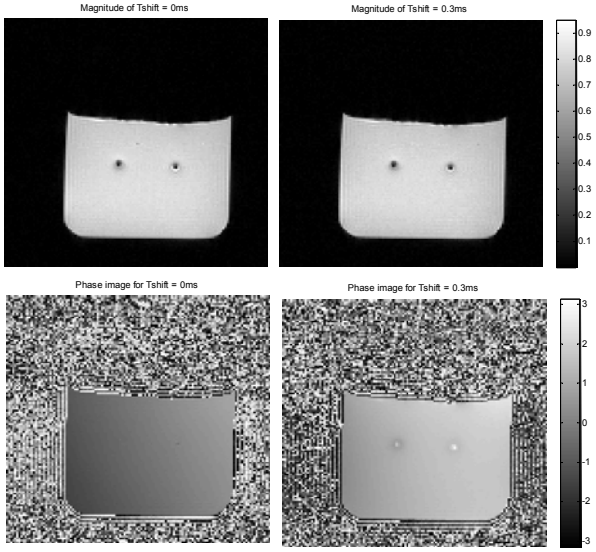

Fig.5 The magnitude images (up) and corresponding phase images (down) of the experimental data in the center slice (slice 4) with Tshift = 0 and 0.3ms.

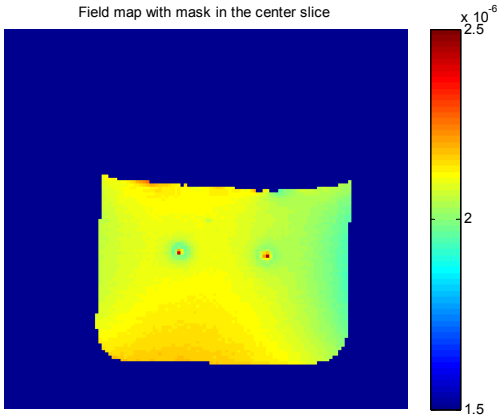

Fig.6 The field map calculated using the experimental data in the center slice (slice 4) with mask.

IV. Discussion

The direct kernel deconvolution in the Fourier domain does not work reliably because it depends on the choice of k-space location. Ill-poseness or ill-condition arises when the Fourier convolution kernel becomes zero, or is very small (close to 0). Only when $k_z << k_x$ and k_y, the very small number can be avoided, but this means the field of view (FOV) on z direction should be significantly larger than FOV on x and y direction which is infeasible in MRI scanner.

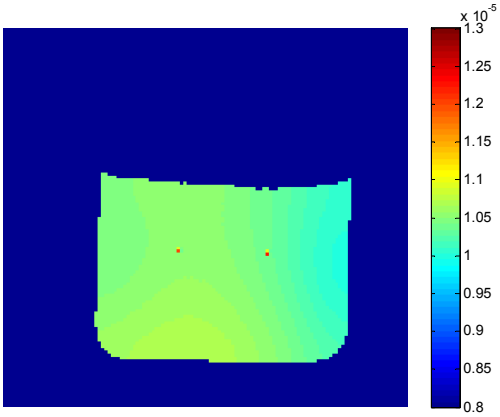

Fig.7 The susceptibility map calculated using the experimental data in the center slice (slice 4).

In the experimental data, the background field is not homogeneous. A gradual changing is observed in the images and the calculated field map. In the susceptibility map, this inhomogeneity is supposed to be removed by the algorithm, however, the result still shows the gradual inhomogeneity. But the field strength change due to the seeds is well removed, and the result shows a clear localization of the seeds and a good homogeneity of the susceptibility.

Susceptibility weighted imaging (SWI) can also be used to locate the seeds. It has computational advantages. However, QSM can provide better location of the seeds, moreover, it can quantitatively measure the susceptibility.

The advantage of using positive contrast in prostate brachytherapy is that it is easy to differentiate. With much higher susceptibility, the seed shows much brighter in the MRI images than any of the human tissues.

The methodology utilized in this paper has been proposed in other applications such as quantitative SWI studies. However, it is the first attempt for positive-contrast brachytherapy seed MRI that we know of.

V. Conclusion

We developed a new method to generate positive contrast MRI of brachytherapy seeds by mapping their susceptibility. The method is based on an improved kernel deconvolution algorithm using l_1 regularization. This is the first attempt to apply the similar technology to brachytherapy seed MRI. Simulation results have shown that the positive contrast seeds can be identified and differentiated using the proposed method. Future work includes validation using tissue-mimic phantom and small animal models.

Acknowledgement

This work was supported in part by the National Science Foundation under award number 0748180. Any opinions, findings and conclusions or recommendations expressed in this material are those of the authors and do not necessarily reflect those of the National Science Foundation.

References

[1] A. V. D'Amico, R. Cormack, C. M. Tempany, S. Kumar, G. Topulos, H. M. Kooy, and C. N. Coleman, "Real-time magnetic resonance image-guided interstitial brachytherapy in the treatment of select patients with clinically localized prostate cancer," *International Journal of Radiation Oncology* Biology* Physics,* vol. 42, pp. 507-515, 1998.

[2] G. Whitehead and J. Ji, "Positive contrast MRI of prostate brachytherapy seeds based on resonant frequency offset mapping," 2010, pp. 6641-6644.

[3] L. de Rochefort, R. Brown, M. R. Prince, and Y. Wang, "Quantitative MR susceptibility mapping using piece‐wise constant regularized inversion of the magnetic field," *Magnetic Resonance in Medicine,* vol. 60, pp. 1003-1009, 2008.

[4] J. D. Jackson and R. F. Fox, "Classical electrodynamics," *American Journal of Physics,* vol. 67, p. 841, 1999.

[5] J. Liu, T. Liu, L. de Rochefort, J. Ledoux, I. Khalidov, W. Chen, A. J. Tsiouris, C. Wisnieff, P. Spincemaille, and M. R. Prince, "Morphology enabled dipole inversion for quantitative susceptibility mapping using structural consistency between the magnitude image and the susceptibility map," *Neuroimage,* 2011.

[6] J. Marques and R. Bowtell, "Application of a Fourier‐based method for rapid calculation of field inhomogeneity due to spatial variation of magnetic susceptibility," *Concepts in Magnetic Resonance Part B: Magnetic Resonance Engineering,* vol. 25, pp. 65-78, 2005.

[7] M. Hanke and P. C. Hansen, "Regularization methods for large-scale problems," *Surv Math Ind,* vol. 3, pp. 253-315, 1993.

[8] B. Kressler, L. de Rochefort, T. Liu, P. Spincemaille, Q. Jiang, and Y. Wang, "Nonlinear regularization for per voxel estimation of magnetic susceptibility distributions from MRI field maps," *Medical Imaging, IEEE Transactions on,* vol. 29, pp. 273-281, 2010.

[9] M. Lustig, D. Donoho, and J. M. Pauly, "Sparse MRI: The application of compressed sensing for rapid MR imaging," *Magnetic Resonance in Medicine,* vol. 58, pp. 1182-1195, 2007.

[10] A. S. Kirov and J. F. Williamson, "Monte-Carlo-aided dosimetry of the Source Tech Medical Model STM1251 I-125 interstitial brachytherapy source," *Med. Phys.,* vol. 28, pp. 764-772, 2001.